Journal of Sound and Vibration (1999) **227**(1), 183–204
Article No. jsvi.1999.2341, available online at http://www.idealibrary.com on IDEAL®

ROBUST CONTROL OF CHAOTIC VIBRATIONS FOR IMPACTING HEAT EXCHANGER TUBES IN CROSSFLOW

J. M. DE BEDOUT, M. A. FRANCHEK AND A. K. BAJAJ

School of Mechanical Engineering, Purdue University, West Lafayette, IN 47907, *U.S.A.*

(*Received* 10 *August* 1998 *and in final form* 16 *April* 1999)

A robust feedback controller design to suppress flutter-type chaotic vibrations in baffled heat exchanger tubes is presented. The vibrations are the result of the fluid dynamic forces on the tube which behave as a negative damping element. A consequence of these vibrations is that the heat exchanger tubes impact with the baffle plates thereby reducing the service life of the heat exchanger. To eliminate the resulting tube impacts, a feedback control strategy is proposed. The heat exchanger tube and the fluid dynamic forces acting on the tube are modeled with linear delayed differential equations. Due to the presence of the delay, these equations do not have a rational realization. The feedback controller is realized using a frequency domain loop shaping approach which is well suited for systems with transcendental transfer functions. The control effector is a magnetic force transducer that acts on the heat exchanger tube. The design strategy is based upon the premise that stabilizing the linear instability about the undeformed tube position will preclude the formation of the nonlinear chaotic vibrations that arise from impacting. The feedback controller is shown to provide robust stability and performance over a large flow velocity regime

1. INTRODUCTION

Heat exchanger tube arrays in fluid crossflows have demonstrated dynamic instabilities for sufficiently large flow velocities. Some of these instabilities have been linked to a negative damping mechanism arising from the fluid dynamic forces acting on the tubes, analogous to single-degree-of-freedom flutter [1]. As the amplitude of tube vibration grows due to the fluid loading, the heat exchanger tubes eventually impact with the oversized holes they are threaded through in the heat-exchanger baffle plates. The function of these baffle plates is to direct the fluid flow and provide support for the heat exchanger tubes. Although the impacting of the tubes and the baffle plates bounds the magnitude of the tube vibration amplitude, it also reduces the life expectancy of the heat exchanger. An approach for designing stabilizing feedback controllers to eliminate these impacting vibrations is presented in this paper.

The non-linear vibrations of heat exchanger tubes in fluid crossflows arise from a fluid-induced dynamic instability [1,2]. Paidoussis and Li [2] demonstrated that chaotic oscillations for such systems are in fact possible for large enough fluid flow

0022-460X/99/410183 + 22 $30.00/0

velocities. In this work, the heat exchanger tube array dynamics are studied by assuming all of the tubes in the array except one to be rigid. The dynamics of the flexible tube are investigated and considered to be characteristic of the entire array. Motion of the flexible tube is assumed to be in the crossflow direction only. The solid–fluid interaction problem of the tube dynamics is modelled by a linear delayed differential equation. The delay term arises due to the fluid forces acting on the tube which are induced by the motion of the tube itself with respect to the viscous wake of neighboring tubes. This partial differential equation can be discretized on a modal basis via a Galerkin expansion [2]. When expressed in state-variable form, the resulting equations of motion have a delayed state vector and therefore the realization of these state equations is an irrational transfer function. The only non-linearity considered by Paidoussis and Li in reference [2] is the impacting force between the baffle plate hole and the heat exchanger tube, which was modelled both a cubic spring and as a trilinear spring. The non-linearities arising from fluid forces are assumed much smaller compared to the structural non-linearity. A more comprehensive model of the system dynamics, which includes the fluid force non-linearities and tube motion in the inflow direction is given in references [3, 4]. An in-depth analysis of the mechanisms leading to chaos in this system is given in reference [5].

The flutter-type oscillations exhibited by the heat exchanger tubes could be eliminated over a wide flow velocity regime using robust stabilizing feedback control. For the purpose of controller design, the impacting between the tube and the baffle plate can be ignored based upon the premise that it provides a restoring force to the tube and serves to enhance the stability [6]. Removing the linear instability via feedback control therefore becomes the primary controller design objective. The controller design methodology must accomodate *internally delayed* systems, which are those systems whose state equations also incorporate delayed states. The process of selecting a design methodology from those available in the literature begins with the selection of either a time or a frequency-domain strategy. Among the time-domain techniques are several linear optimal methods and a variable structure control methodology known as sliding mode control (SMC). Several H^{∞} optimal control methods and classical frequency response loop shaping are available for a frequency domain design.

Chyung and Lee [7], and Koivo and Lee [8] investigated the application of linear optimal methods having quadratic and other convex cost functionals for time-varying internally delayed systems. These are full-state feedback methods and thus require state observers if all states are not measurable. This increases the controller design's dependence on accurate system models and increases implementation complexity. The issue of robustness with respect to model uncertainty is another significant problem facing this class of design methods. For example, in Yau *et al.* [6] the application of an LQG controller to a discretized distributed parameter system similar to the one considered in this paper had small stability margins in the face of relatively small parameter uncertainty.

Another time-domain contoller design methodology recently applied to internally delayed systems is SMC. Recent work by Luo *et al.* [9, 10] has shown the application of SMCs to parametric uncertain internally delayed systems.

Furthermore, both full-state feedback and output feedback implementations are considered. However, due to the switching nature of SMC controllers, the closed-loop systems exhibit chattering during system transients. In general, switching type control laws have high controller bandwidths thereby making the closed-loop systems susceptible to actuator rate saturation and senior noise.

In the frequency domain, several H^∞ optimal control methods are capable of synthesizing controllers for internally delayed systems. In references [11, 12], robust H^∞ full-state feedback controllers for state delayed systems with parametric and structured uncertainty are developed. Both methods require the solution of Riccati inequalities. The synthesized controllers are contingent upon the selection of appropriate positive-definite matrices. In Toker and Ozbay [13], an output feedback strategy for the mixed sensitivity problem in SISO systems which can have transcendental transfer functions is developed. The method allows for the direct computation of optimal and suboptimal controllers by solving a finite set of linear homogeneous equations. However, the solution requires a factorization of the plant into inner and outer parts that can be difficult for complicated systems.

A 1940s based classical controller design methodology can be extended to internally delayed systems that are described by transcendental transfer functions. This design methodology is the so-called loop-shaping approach. Closed-loop stability can be guaranteed for linear systems using the Nyquist encirclement condition [14]. A distinction between loop-shaping and the other controller design methodologies discussed previously is the manner in which closed-loop performance is addressed. Closed-loop frequency domain performance specifications and system uncertainty can be transparently displayed on the open-loop gain-phase plane. In addition, certain types of time-domain performance specifications can be enforced via amplitude inequalities in the frequency domain [15]. In contrast, the optimal control methodologies discussed previously make use of weighting functions or matrices to address performance. Iteration of these performance weights is usually required to converge to an acceptable performance.

To demonstrate the loop-shaping approach, a stabilizing controller that is robust with respect to variations in the fluid flow velocity is designed to suppress the flutter-type behavior in heat exchanger tubes. To accomplish this design, a stability analysis of the tube using the models developed by Paidoussis and Li in reference [2] is first presented to identify the stable and unstable flow velocity regimes. A state variable model that includes the effect of a control actuator is then developed. A constant coefficient controller is designed based on these models to suppress the non-linear vibrations over a wide flow velocity range. The premise behind the controller design is that removing the linear instability induced by the fluid dynamic forces on the tube will eliminate the non-linear vibrations resulting from tube and baffle impacting. The effectiveness of the controller in suppressing undesirable oscillations is demonstrated through numerical simulations.

2. SYSTEM DYNAMICS AND STABILITY

An analytical model for a two-span heat exchanger tube subject to a fluid crossflow was developed by Paidoussis and Li [2]. A synopsis of this model

development is reviewed in this section. Following this development is a dynamic analysis of the model. System simulations involving a wide flow velocity range serve to illuminate stable and unstable flow velocity regimes.

2.1. MODEL DEVELOPMENT

Consider the two-span heat exchanger tube in crossflow in Figure 1. The ends of the tube are rigidly supported and the position on the baffle plate relative to the heat exchanger lower wall is denoted as x_b. It is assumed that the heat exchanger tube moves perpendicular to the flow direction only. While inflow motion of the tube does occur in real systems, the tube response is usually dominant in the crossflow direction [1, 3]. The following derivation of the equation of motion for the heat exchanger tube subjected to crossflow is developed in Paidoussis and Li [2] and outlined here.

The dynamics of the tube in fluid crossflow are described by

$$EI\frac{\partial^4 w}{\partial x^4} + c\frac{\partial w}{\partial t} + m\frac{\partial^2 w}{\partial t^2} + \delta(x - x_b)f(w) = F(w, \dot{w}, \ddot{w}), \tag{1}$$

where w denotes the displacement of the tube perpendicular to the flow direction, EI is the flexural rigidity of the tube, c is the damping coefficient, m is the tube mass per unit length, x denotes the position along the tube relative to the lower wall, δ is the Dirac delta function, f is the force exerted by the baffle on the tube, and F is the

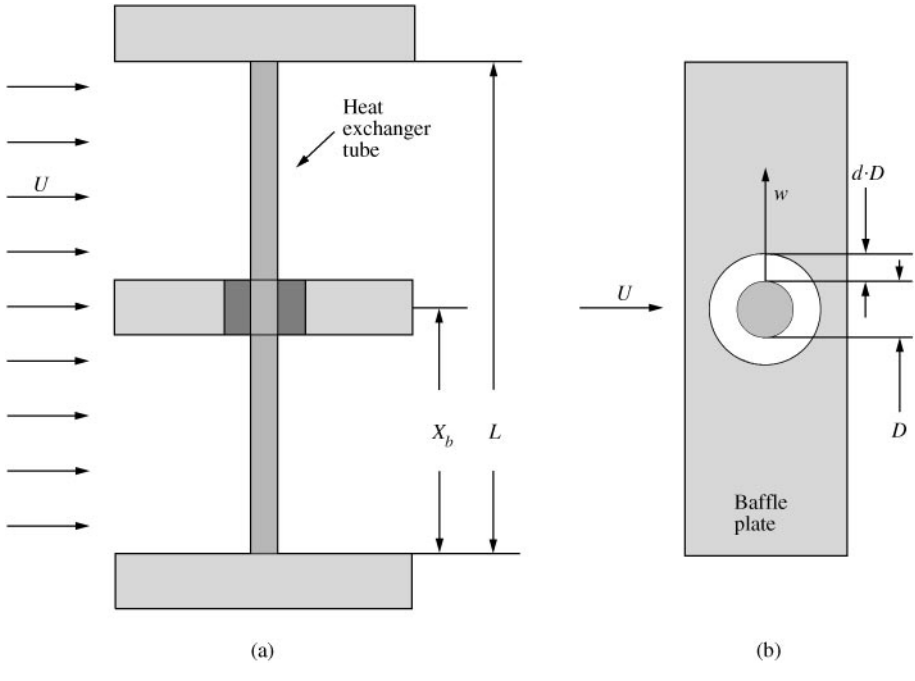

Figure 1. Heat exchanger tube subjected to fluid cross flow: (a) top view, (b) side view.

force induced by the crossflow on the tube. The crossflow-induced force F is a function of the tube motion and may be written as [2]

$$F(w, \dot{w}, \ddot{w}) = M\frac{\partial^2 w}{\partial t^2}(x, t) + B\frac{\partial w}{\partial t}(x, t) + Cw(x, t - \Delta t), \tag{2}$$

where

$$M = -\frac{\pi}{4}\rho D^2 C_{ma}, \quad \mathrm{B} = -\frac{1}{2}\rho \mathrm{UDC}_D, \quad \mathrm{C} = \frac{1}{2}\rho U^2 D\frac{\partial C_L}{\partial w}, \quad \Delta t = \mu\frac{D}{U}.$$

The variable D is the tube diameter, ρ the fluid density, U the velocity of the crossflow fluid, C_D and C_L the drag and lift coefficients, respectively, C_{ma} the *added* mass coefficient of the fluid around the cylinder, and Δt the delay between tube motion and the fluid dynamic forces generated from these motions.

Consider the following dimensionless quantities, where L describes the length of the heat exchanger tube and λ_1 is the dimensionless eigenvalue of the first mode for a beam rigidly supported at both ends:

$$\eta = \frac{w}{D}, \quad \xi = \frac{x}{L}, \quad \tau = \lambda_1^2\sqrt{\frac{EI}{mL^4}}t = \Omega_1 t, \quad \zeta = \frac{c}{m\Omega_1},$$

$$\tilde{m} = \frac{m}{\rho D^2}, \quad \tilde{U} = \frac{2\pi U}{D\Omega_1}, \quad \tilde{f} = \frac{f}{m\Omega_1^2 D}, \quad \beta = \left(1 + \frac{4\tilde{m}}{\pi C_{ma}}\right)^{-1}. \tag{3}$$

Substituting the dimensionless variables (3) and the fluid force (2) into the tube equation (1) yields the dimensionless equation

$$\frac{1}{1-\beta}\frac{\partial^2\eta}{\partial\tau^2}(\xi, \tau) + \left(\zeta + \frac{\tilde{U}C_D}{4\pi\tilde{m}}\right)\frac{\partial\eta}{\partial\tau}(\xi, \tau) + \frac{1}{\lambda_1^4}\frac{\partial^4\eta}{\partial\xi^4}(\xi, \tau) - \frac{\tilde{U}^2}{8\pi^2\tilde{m}}\frac{\partial C_L}{\partial\eta}\eta(\xi, \tau - T)$$
$$+ \delta(\xi - \xi_b)\tilde{f}(\eta) = 0. \tag{4}$$

In this equation, T is the dimensionless delay time given by

$$T = \frac{2\pi}{\tilde{U}} \tag{5}$$

for $\mu = 1$.

To study the dynamics of the tube subject to crossflow, it is convenient to reduce the model to a finite size via Galerkin approximation of the tube model. The basis functions for the Galerkin expansion can be chosen to be the eigenfunctions of the linear tube problem without the time delay. For this purpose, note that the dimensionless modal eigenvalues λ_i for a tube rigidly supported at both ends are given by the solutions of

$$\cosh(\lambda_i)\cos(\lambda_i) = 1. \tag{6}$$

The corresponding eigenfunctions for the tube with rigid supports are

$$\phi_i(\xi) = C_{1_i}[\cosh(\lambda_i\xi) - \cos(\lambda_i\xi)] + C_{2_i}[\sinh(\lambda_i\xi) - \sin(\lambda_i\xi)], \tag{7}$$

where C_{1_i} and C_{2_i} are found for each mode of the beam by using the boundary conditions

$$\phi_i(0) = \frac{\partial \phi_i}{\partial \xi}(0) = \phi_i(1) = \frac{\partial \phi_i}{\partial \xi}(1) = 0$$

and the normalization

$$\int_0^1 \phi_i(\xi)\phi_j(\xi)\,\mathrm{d}\xi = \begin{cases} 1, & \text{for } i = j, \\ 0, & \text{for } i \neq j. \end{cases} \tag{8}$$

Using the above defined basis functions, the non-linear system (4) can now be discretized via a standard Galerkin expansion [2]:

$$\eta(\xi, \tau) = \sum_{i=1}^{N} \phi_i(\xi) q_i(\tau), \tag{9}$$

where the $q_i(\tau)$ terms describe the time-dependent contribution from each mode to the overall tube response $\eta(\xi, \tau)$. The $\phi_i(\xi)$ are the normalized eigenfunctions specified by equation (7). Substituting equation (9) into equation (4), multiplying by $\phi_j(\xi)$ and integrating over $\xi \in [0, 1]$ gives the discretized equations of motion,

$$\frac{1}{1-\beta}\ddot{q}_i(\tau) + \left(\frac{\delta_i v_i}{\pi} + \frac{\tilde{U} C_D}{4\pi\tilde{m}}\right)\dot{q}_i(\tau) + v_i^2 q_i(\tau) - \frac{\tilde{U}^2}{8\pi^2\tilde{m}}\frac{\partial C_L}{\partial \eta} q_i(\tau - T) + \tilde{f}(\eta_b)\phi_i(\xi_b) = 0, \quad i \in I_{+/(N+1)}, \tag{10}$$

where $v_i = (\lambda_i/\lambda_1)^2$, η_b is the displacement at $\xi = \xi_b$, and the viscous damping term has been replaced by the modal damping $\delta_i v_i/\pi$. The only variable parameter in this work is the dimensionless flow velocity $\tilde{U}$. The fixed values for the other parameters were chosen in accordance to those used in reference [2]:

$$\beta = 0{\cdot}24, \quad \delta_i = 0{\cdot}06, \quad C_D = 0{\cdot}26, \quad \tilde{m} = 3, \quad \frac{\partial C_L}{\partial \eta} = -8.1.$$

These values correspond to a square heat exchanger tube array with center-to-center pitch-to-diameter ratio $p/D = 1{\cdot}5$ [2].

The tube and baffle impact force $\tilde{f}(\eta_b)$ is modelled as a cubic spring (see Figure 2),

$$\tilde{f}(\eta_b) = \kappa \eta_b^3, \tag{11}$$

where κ is the stiffness of the cubic spring. In this work, $\kappa = 1000$ in accordance with reference [2], and the location of the baffle plate is at $\xi_b = 0{\cdot}5$. This approximation to the real constraint force, which behaves more as a trilinear spring, is made for analysis purposes. The bifurcation diagrams that will be generated for this system in the following section will be cleaner and easier to interpret with the cubic model due to the smoothness of the force transition through the impact point. Ultimately, however, simulations for the controlled system will be provided with both the cubic and trilinear spring models. The trilinear spring model is

$$\tilde{f}(\eta_b) = \kappa[\eta_b - \tfrac{1}{2}(|\eta_b + d| - |\eta_b - d|)], \tag{12}$$

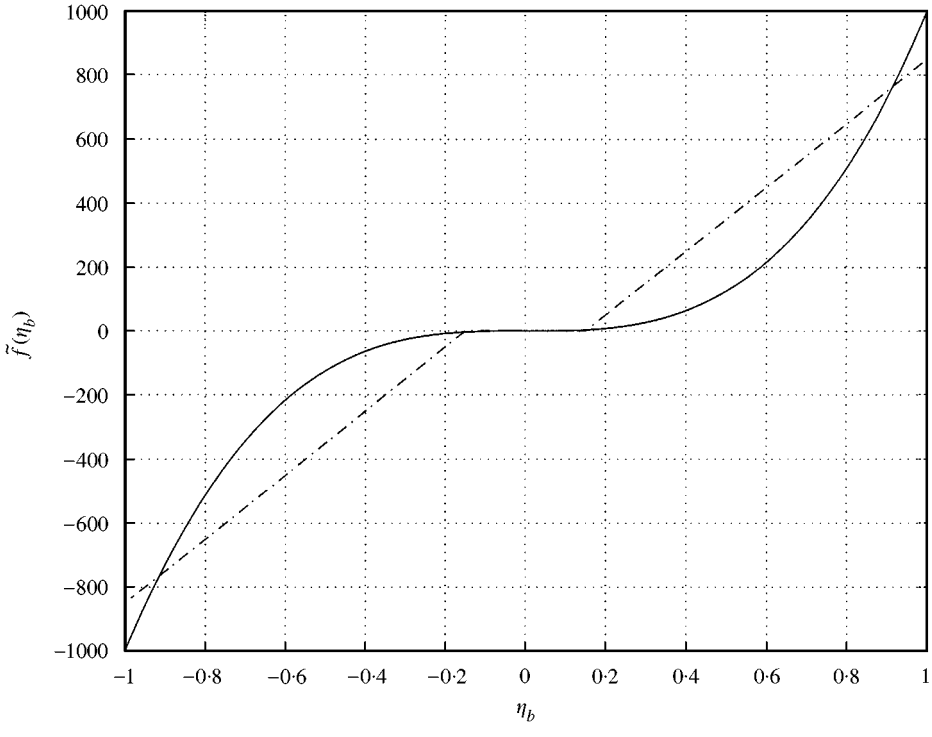

Figure 2. Spring models of the baffle plate constraint force: ——, cubic model; —·—, trilinear model.

where $2d$ is the gap width between the baffle plate hole and the tube, non-dimensionalized by D [2]. For this work, $\kappa = 1000$ and $d = 0{\cdot}15$. The gap width d is larger than the one used in reference [2], to allow larger amplitude oscillations. This model is more accurate than the cubic spring model since the force exerted on the tube while inside the gap is zero (Figure 2). In addition, the force exerted upon impact of the tube and the baffle is larger for the trilinear spring model.

Note that the baffle has been located at the midpoint along the tube. This implies that the even modes of the tube have a node at $\xi = \xi_b$ and may not contribute to the tube displacement at ξ_b depending on whether the response of the tube is symmetrical or asymmetrical. Paidoussis and Li [2] have also studied the more general case when $\xi_b \neq 0{\cdot}5$. Also, note that equations (10) are a system of N second order non-linear delayed differential equations. Interestingly, the only coupling between the various modal amplitudes arises due to the constant force $\tilde{f}(\eta_b)$ of the baffle support.

2.2. STABILITY ANALYSIS

Paidoussis and Li [2] proposed that the first five discrete modes of equation (10) are sufficient to describe the heat exchanger tube dynamics. Equation (10) may be expressed in stable variable form,

$$\dot{\mathbf{y}} = \mathbf{A}_0 \cdot \mathbf{y} + \mathbf{A}_1 \cdot \mathbf{y}(\tau - T) + \mathbf{B}_0 \cdot \tilde{f}(\eta_b), \tag{13}$$

where

$$\mathbf{y} = [q_1\ \dot{q}_1\ q_2\ \dot{q}_2\ q_3\ \dot{q}_3\ q_4\ \dot{q}_4\ q_5\ \dot{q}_5]^{\mathrm{T}}.$$

A linear stability analysis of the static equilibrium at $\mathbf{y} = \mathbf{0}$ has been conducted in reference [2]. Their analysis shows that each of the modes of vibration for the tube lose stability as the flow rate $\tilde{U}$ is quasi-statically increased. Recall that the modal amplitudes q_i are uncoupled in the absence of any non-linearity. It turned out that the lowest beam mode becomes unstable at the lowest critical flow rate. Each of the successively higher modes becomes unstable at a higher flow rate. The loss of stability in each case is due to a pair of complex eigenvalues moving into the right half-plane with non-zero imaginary parts. With this picture in mind, the non-linear system described by equation (13) was simulated in MATLAB for the flow-velocity range $\tilde{U} \in [0, 7]$ with various initial conditions. The integration step size was 0·01 dimensionless time units (dtu).

The first set of simulations investigated the stability of the non-linear system over the previously described flow velocity regime for small initial conditions. Specifically, initial conditions of $\eta_b = 0{\cdot}0048$ and $\dot{\eta}_b = 0$ for $-T \leqslant \tau \leqslant 0$ were used. This is analogous to releasing the tube from a fixed position. For each flow velocity, simulations for 2000 dtu's were performed. The last 50 dtu's of these simulations give the steady-state response. The bifurcation diagram generated for this set of simulations for the steady-state behavior where $\dot{\eta}_b = 0$ is shown in Figure 3.

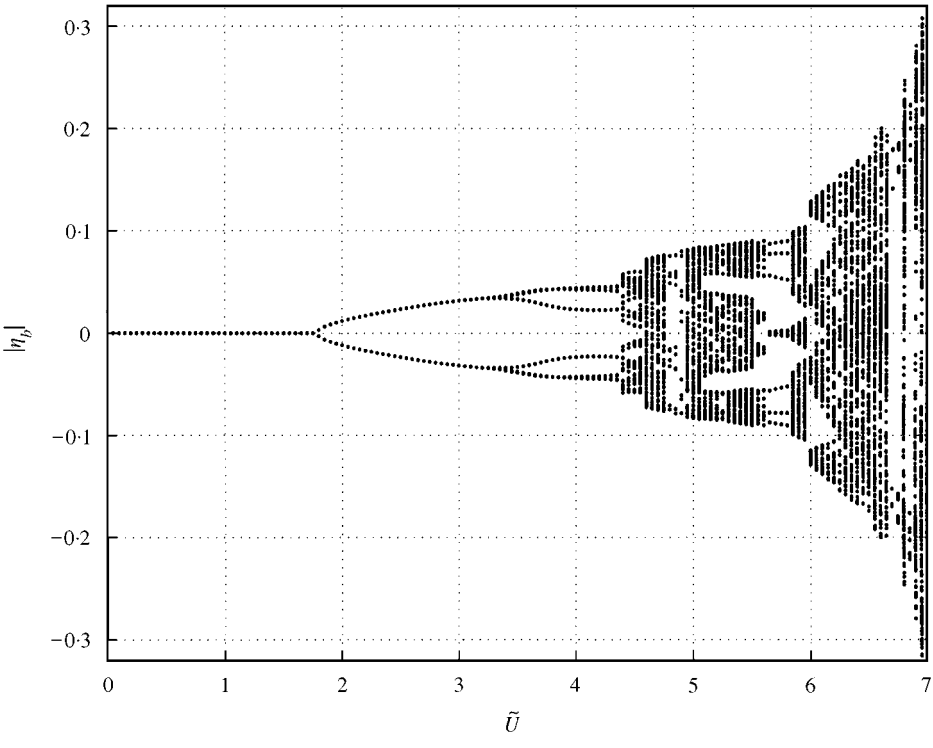

Figure 3. Bifurcation diagram for small initial conditions.

For $\tilde{U} \leqslant 1{\cdot}75$, the undeformed position at $\xi = \xi_b$ is stable (Figure 3). At $\tilde{U} \cong 1{\cdot}8$, the undeformed position becomes an unstable equilibrium point via a Hopf bifurcation, and stable limit cycles form for flow velocities up to $\tilde{U} \cong 4{\cdot}4$. At $\tilde{U} \cong 3{\cdot}25$, a post-Hopf bifurcation occurs. For $\tilde{U} \geqslant 4{\cdot}4$, chaotic oscillations occur with sporadic windows of periodic oscillations. This bifurcation diagram concurs with the one generated in reference [2].

A second set of simulations with larger initial conditions investigated the uniqueness of the bifurcation diagram in Figure 3. For initial conditions of $\eta_b = 0{\cdot}159$ and $\dot{\eta}_b = 0$ during $-T \leqslant \tau \leqslant 0$, simulations were repeated for each flow velocity over the considered regime. The last 50 dtu's were again considered the steady-state response. However, two flow velocity regions inside $\tilde{U} \in [0{\cdot}7, 2]$ displayed steady-state amplitudes of vibration that are markedly different from those seen with smaller initial conditions. Simulations over this flow velocity region were repeated with a higher resolution in $\tilde{U}$ and over a time period of 5000 dtu's to ensure that the behavior seen was not a transient event. The last 50 dtu's were considered steady-state behavior. The bifurcation diagram formed by splicing the appropriate sections of the large initial condition simulations together is shown in Figure 4. The first additional branch arises for $\tilde{U} \in [0{\cdot}945, 1{\cdot}165]$, whereas the second branch arises for $\tilde{U} \in [1{\cdot}72, 1{\cdot}92]$. The appearance of these new branches was not reported in reference [2], and they are not predicted by a stability analysis of the linearized system disregarding the non-linear baffle force. Price and Valerio

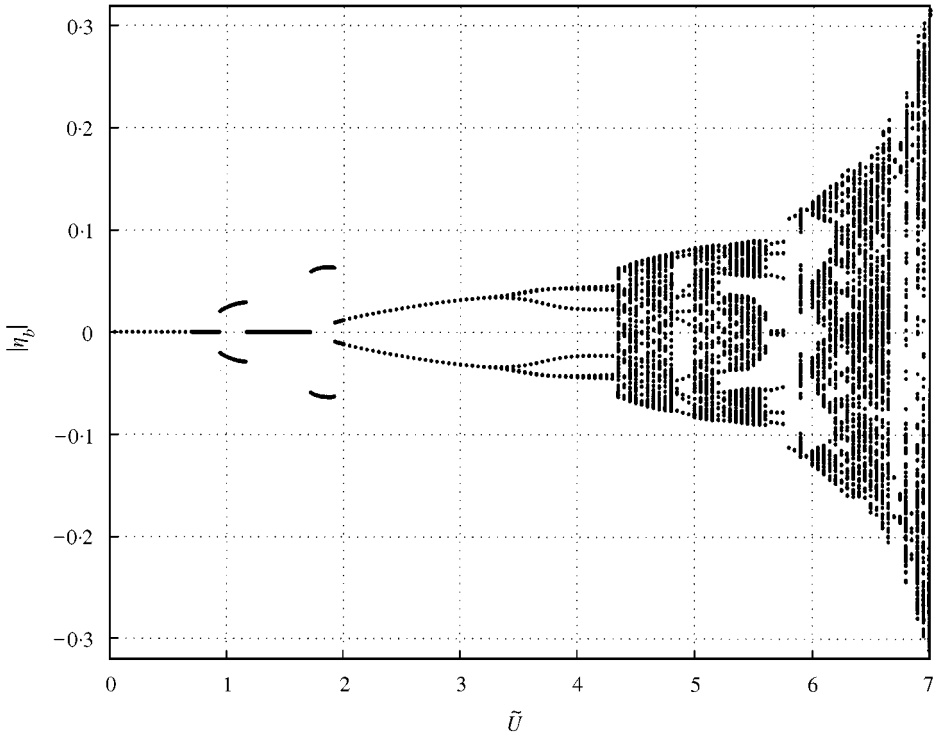

Figure 4. Bifurcation diagram for large initial conditions.

[1] discuss how multiple solutions can exist for the limit cycle amplitude in a non-linear system. The system considered in reference [1] is also a constrained flexible pipe in fluid crossflow, although the non-linearity considered is in the fluid forces acting on the tube and not the result of baffle impacting. The behavior of the bifurcation diagram for $\tilde{U} \in [2, 4{\cdot}3]$ was identical to that displayed in Figure 3 for smaller initial conditions. The onset of chaos for larger initial conditions occurs at $\tilde{U} \cong 4{\cdot}35$, which is slightly lower than that seen for smaller initial conditions.

The smaller initial condition bifurcation diagram allows for the identification of the flow velocities that possess the fluid dynamic instability responsible for the tube vibration. This is useful for controller design purposes, since it separates the flow velocities that need a stabilizing controller from those that only require performance enhancement. The large initial condition bifurcation diagram indicates that there may be two flow velocity regimes where a linear controller design might not provide stability or performance enhancement of the closed-loop system.

3. MODEL AUGMENTATION

The model presented in section 2.1 is now augmented with actuator and sensor dynamics for the purpose of feedback control. For the present work, it is assumed that there is a displacement sensor located at $\xi = \xi_b$, the location of the baffle. The control effector is a magnetic force actuator located at $\xi = \xi_c$. For generality, it is assumed that $\xi_c \neq \xi_b$. The control problem is thus non-collocated, meaning that the position of ξ_b is being regulated with an actuator at a different location.

The Laplace transform of the actuator dynamics are assumed to be of the form

$$\frac{u(s)}{u_c(s)} = \frac{1}{(s/\gamma + 1)}, \tag{14}$$

where $u(s)$ denotes the dimensionless actuator force, $u_c(s)$ is the control signal sent to the actuator and γ imposes a bandwidth limitation on actuation. The value of γ is chosen as 60 rad/dtu, which is higher than the resonant peaks of the plant dynamics being considered (see Figure 5 for a Bode plot of the family of plants for $\tilde{U} \in [0, 7]$). This ensures adequate control bandwidth and reduces the risk of actuator rate saturation.

Modifying equation (4) to include the effects of the actuator force at $\xi = \xi_c$ yields the discretized equations of motion

$$\frac{1}{1-\beta}\ddot{q}_i(\tau) + \left(\frac{\delta_i v_i}{\pi} + \frac{\tilde{U} C_D}{4\pi\tilde{m}}\right)\dot{q}_i(\tau) + v_i^2 q_i(\tau) - \frac{\tilde{U}^2}{8\pi^2\tilde{m}}\frac{\partial C_L}{\partial \eta} q_i(\tau - T) + \tilde{f}(\eta_b)\phi_i(\xi_b)$$
$$= u(\tau)\phi_i(\xi_c), \quad i \in I_{+/(N+1)}. \tag{15}$$

The dimensionless actuator force $u(\tau)$ is

$$u(\tau) = \frac{\Gamma(\tau)}{m\Omega_1^2 D}, \tag{16}$$

where $\Gamma(\tau)$ is the dimensional force exerted by the actuator at $\xi = \xi_c$. Equation (15) may be expressed in state variable form as

$$\dot{\mathbf{y}} = \mathbf{A_0}\cdot\mathbf{y} + \mathbf{A_1}\cdot\mathbf{y}(\tau - T) + \mathbf{B_0}\cdot\tilde{f}(\eta_b) + \mathbf{B_1}\cdot u(\tau), \quad \eta(\xi_b) = \mathbf{C}\cdot\mathbf{y}, \tag{17}$$

where C is of dimension $(1 \times 2N)$.

Selecting the location of ξ_c influences the controller design. For example, mounting the actuator at the location of a modal node would preclude the use of that mode in controlling the vibration at ξ_b. For this study, the actuator is located at $\xi_c = 0{\cdot}45$ which is close to the desired control location ξ_b and does not lie on any of the modal nodes for the first five modes.

4. FEEDBACK CONTROLLER DESIGN

The design of a stabilizing feedback controller for heat exchanger tubes subject to a fluid crossflow with an unknown but bounded flow velocity is presented in this section. Two key issues complicate the design process. The presence of a delayed state vector in equation (17) causes the system transfer function to be transcendental with the consequence that identifying open-loop unstable singularities becomes more difficult. Also, the two additional limit cycle branches in Figure 4 that were not predicted by a linearized stability analysis of the system make it necessary to verify closed-loop stability over these flow regimes via simulation.

4.1. FREQUENCY RESPONSE GENERATION

The transfer function between $\eta_b(s)$ and the actuator force $u(s)$ is obtained by taking the Laplace transform of equation (17):

$$P(s) = \frac{\eta_b(s)}{u(s)} = \mathbf{C}[s\mathbf{I} - \mathbf{A}_0 - \mathbf{A}_1 e^{-\tau s}]^{-1}\mathbf{B}_1. \tag{18}$$

Similarly, the transfer function between $\eta_b(s)$ and the baffle force $\tilde{f}(s)$ is

$$P_d(s) = \frac{\eta_b(s)}{\tilde{f}(s)} = \mathbf{C}[s\mathbf{I} - \mathbf{A}_0 - \mathbf{A}_1 e^{-\tau s}]^{-1}\mathbf{B}_0. \tag{19}$$

The frequency responses of equations (18) and (19) are obtained by substituting $s = j\omega$, where $j = \sqrt{-1}$ and ω is in rad/dtu.

The Bode plot of the family of transfer functions $P(j\omega)$ described by equation (18) for $\tilde{U} \in [0, 7]$ is shown in Figure 5. Two major trends, delineated by phase, can be observed. The phase curves with the greatest lag correspond to $\tilde{U} \in [0, 1{\cdot}75]$. The magnitude versus phase characteristics for this family of plants indicates that the system is stable over this flow regime. This result is verified by the stability analysis of the previous section. The remaining phase curves correspond to $\tilde{U} \in (1{\cdot}75, 7]$. The phase characteristics associated with the underdamped resonant peak at $\omega \cong 0{\cdot}8$ rad/dtu indicate that the complex poles associated with this resonant peak are either marginally stable or unstable. This also is in agreement with the results

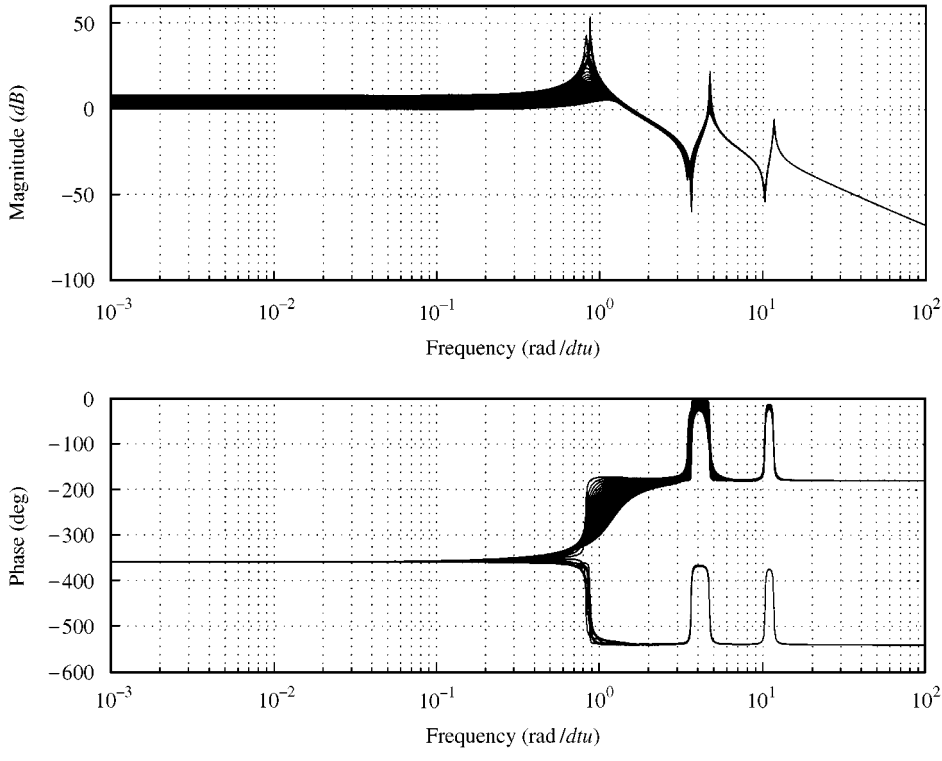

Figure 5. Bode plots of the transfer function between $\eta_b(s)$ and $u(s)$.

from the previous section. No additional unstable singularities occur for equations (18) and (19) over the $\tilde{U}$ range considered, including the flow velocity ranges where the two additional bifurcation branches were discovered.

4.2. LOOP SHAPING THE CONTROLLER

Using unity feedback, the relationship between the the actuator force $u(s)$ and the dimensionless displacement $\eta_b(s)$ is

$$u(s) = -G(s) \cdot \eta_b(s). \tag{20}$$

Note that equation (20) includes the actuator dynamics (14) in the controller $G(s)$. The block diagram for this regulating system is shown in Figure 6. Note that the baffle plate constraint force acts as an output disturbance to the controlled loop. However, the effect of the baffle force is to restore η_b to the equilibrium point, enhancing regulation. Therefore, the controller design will be limited to achieving stabilization of the uncertain linear system $P(s)$ disregarding the effect of the baffle force. A similar approach is advanced in Yau *et al.* [6].

The transmission of the baffle impact force to the system output η_b can be identified from the block diagram in Figure 6. The open-loop transfer function of

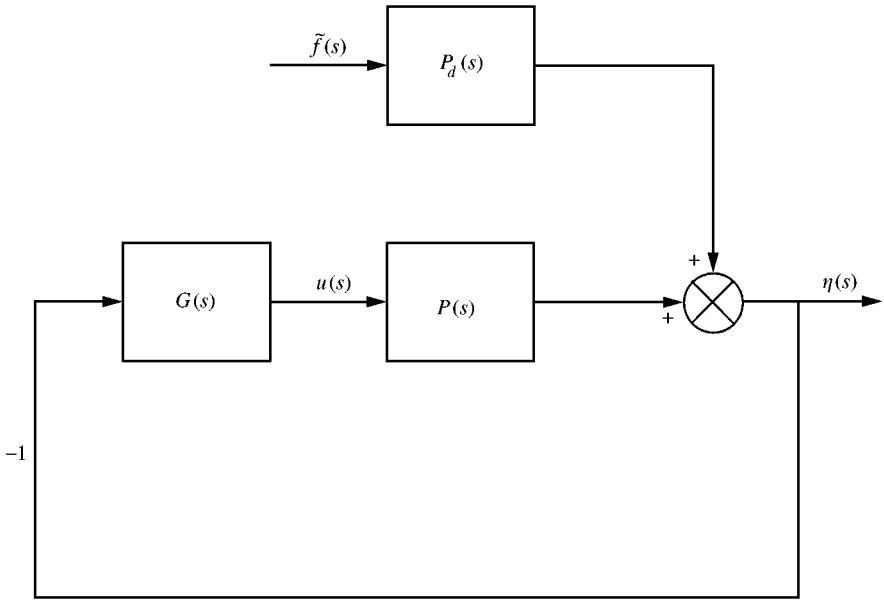

Figure 6. Block diagram of the proposed regulating system.

the regulating system is given by

$$L(s) = G(s) \cdot P(s). \tag{21}$$

The transfer function relating $\eta_b(s)$ to the baffle impact force $\tilde{f}(s)$ is

$$\frac{\eta_b(s)}{\tilde{f}(s)} = P_d(s) \cdot S(s), \tag{22}$$

where $S(s)$ is the closed-loop sensitivity transfer function, defined by

$$S(s) = \frac{1}{1 + L(s)}. \tag{23}$$

The closed-loop sensitivity transfer function therefore provides a a measure of how the closed-loop system will react to the baffle plate impact disturbance. It would be desirable to reduce the magnitude of the the sensitivity transfer function as much as possible to minimize the effect of $\tilde{f}(s)$ on $\eta_b(s)$. However, from the Bode sensitivity integral [16], reducing the closed-loop sensitivity over all frequencies is not possible with a strictly proper controller.

The design of a stabilizing constant coefficient linear controller $G(\mathrm{j}\omega)$ for this system is achieved by shaping the family of open-loop frequency responses defined by

$$L(j\omega) = G(\mathrm{j}\omega) \cdot P(\mathrm{j}\omega) \tag{24}$$

such that $L(\mathrm{j}\omega)$ satisfies the Nyquist encirclement condition. The stable plant set for $\tilde{U} \in [0, 1.75]$ requires no encirclements of the critical point since all singularities for this subset of $P(s)$ are stable. On the other hand, the unstable plant set for

$\tilde{U} \in (1{\cdot}75, 7]$ requires two counter-clockwise encirclements of the critical point in the $L(s)$ plane due to the two unstable poles that exist for this subset of $P(s)$. The effects of the additional branches of the bifurcation diagram that were discovered for large initial conditions in Section 2 will be neglected since they are not present in the frequency responses of equations (18) and (19). The stability over these portions of the flow regime will therefore need to be demonstrated via numerical simulations.

The only performance specification placed on the design is a peak magnitude condition on the closed-loop sensitivity. This peak is specified as 3 dB for all plants in the uncertain set. The 3 dB bound on the peak magnitude of the closed-loop sensitivity limits the reaction of the closed-loop system to the baffle plate impact force. In addition, it directly enforces a certain degree of closed-loop stability by ensuring ample gain and phase separation between the family of loop transmission functions and the critical point.

The design of a robust controller for the flow regime $\tilde{U} \in [0, 7]$ must integrate the stability and performance requirements of the plant set for $\tilde{U} \in (1{\cdot}75, 7]$ with the performance needs of the plant set corresponding to $\tilde{U} \in [0, 1{\cdot}75]$. From Figure 5 it is evident that the only qualitative difference between the stable and unstable plant sets is the 360° phase differential that occurs after the first resonance, at $\omega \cong 0{\cdot}8$ rad/dtu. The open-loop gain-phase plots of the unstable and stable families of frequency responses with closed-loop sensitivity grids are shown in Figures 7

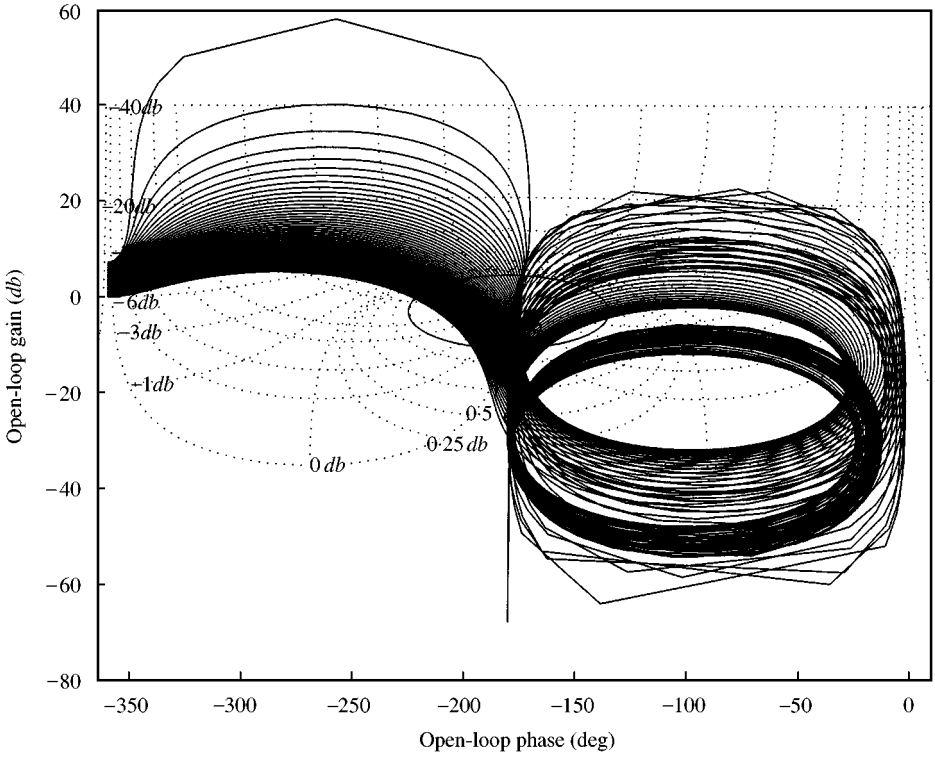

Figure 7. Gain-phase plot of the uncompensated loop transmission functions for $\tilde{U} \in (1{\cdot}75, 7]$.

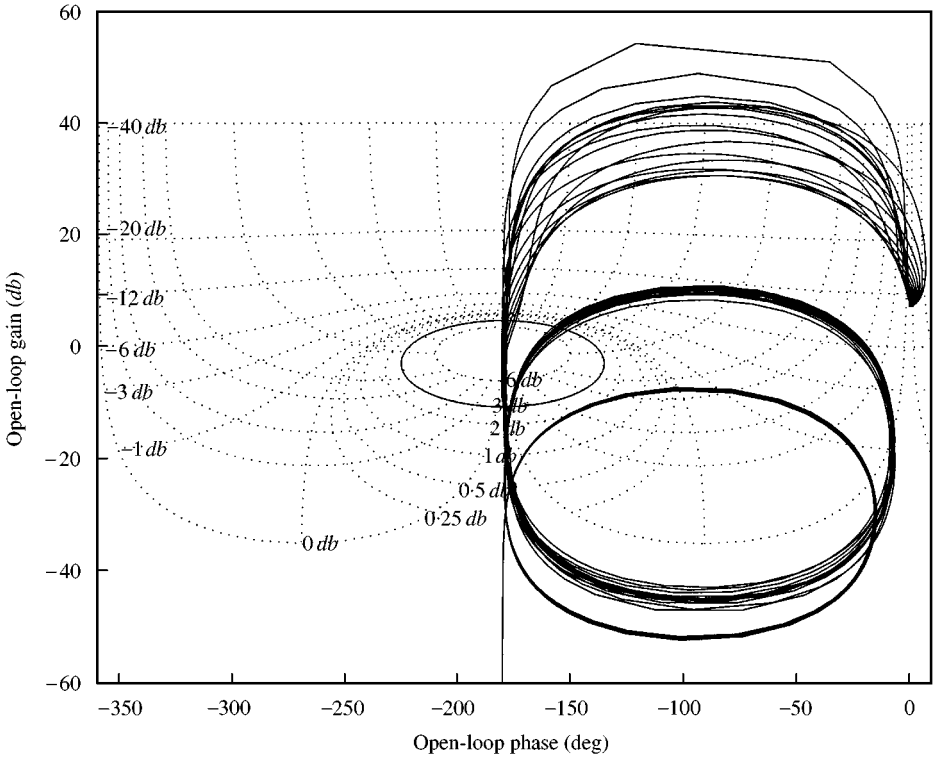

Figure 8. Gain-phase plot of the uncompensated loop transmission functions for $\tilde{U} \in [0, 1{\cdot}75]$.

and 8. Any controller features beyond $\omega \cong 2$ rad/dtu will modify both the stable and unstable plant set frequency responses in the same qualitative manner. The key controller design frequency range is thus $\omega \in [0, 2]$ rad/dtu. Over this frequency range, the controller must stabilize the plant set for $\tilde{U} \in (1{\cdot}75, 7]$ while retaining the stability of the plant set for $\tilde{U} \in [0, 1{\cdot}75]$. According to the Nyquist encirclement condition, the mapping in the $L(s)$ plane of the Nyquist contour must encircle the critical point two times to achieve closed-loop stability of the unstable plant set. Therefore, one encirclement of the critical point is required for $L(j\omega)$ over $\omega \in [0, \infty]$ for the unstable plant set, which is accomplished by adding phase lead and gain to $L(j\omega)$ near the first resonance. Since the stable plant set requires no encirclements of the critical point for closed-loop stability, this control action will also improve the stability of the stable plant set by increasing the separation between the family of loop transmission functions and the critical point (Figure 8). Therefore, a controller designed to stabilize and enhance the performance of the unstable plant set will also improve the stability and performance of the stable plant set.

The controller design is realized by loop shaping the family of frequency responses for $\tilde{U} \in (1{\cdot}75, 7]$ on the open-loop gain-phase plane. Recall from equation (20) that the actuator dynamics are included in the controller. Therefore, the actuator dynamics (14) are first added to the system frequency responses. For closed-loop stability, a gain of -43 dB and phase lead at $\omega = 0{\cdot}2$ and

$\omega = 3$ rad/dtu are added to obtain the required encirclement of the critical point by the family of loop transmission functions near the first resonance. Then, complex zeros at $\omega = 11{\cdot}66$ rad/dtu and complex poles at $\omega = 10{\cdot}27$ rad/dtu are added to cancel the resonances and antiresonances in the plant dynamics at these frequencies (see Figure 5). Complex zeros at $\omega = 5{\cdot}92$ rad/dtu and two simple poles at $\omega = 20$ rad/dtu add phase lead to $L(j\omega)$ at $\omega = 11$ rad/dtu to achieve satisfaction of the 3 dB maximum closed-loop sensitivity performance specification by the family of loop transmission functions. Two high-frequency poles at $\omega = 20$ rad/dtu are then added to make the controller strictly proper and achieve a higher amplitude roll-off for sensor noise attenuation. The open-loop gain-phase plots of the family of compensated transfer functions for this flow regime and for the plants in $\tilde{U} \in [0, 1{\cdot}75]$ are shown in Figures 9 and 10, respectively. Since both plant sets are closed-loop stable and meet the performance specifications, this robust control law can be used to regulate $\eta(\xi_b)$ over the entire flow velocity regime $\tilde{U} \in [0, 7]$ without the need to sense the fluid flow velocity. The transfer function of the designed controller is

$$G(s) = \frac{2400000(s + 0{\cdot}008)(s + 2)(s^2 + 0{\cdot}2s + 135{\cdot}8530)(s^2 + 1{\cdot}9s + 35)}{(s + 60)(s^2 + 10s + 25)(s^2 + 0{\cdot}2s + 105{\cdot}3805)(s^2 + 40s + 400)(s^2 + 40s + 400)}. \tag{25}$$

The Bode plot of $G(s)$ is shown in Figure 11.

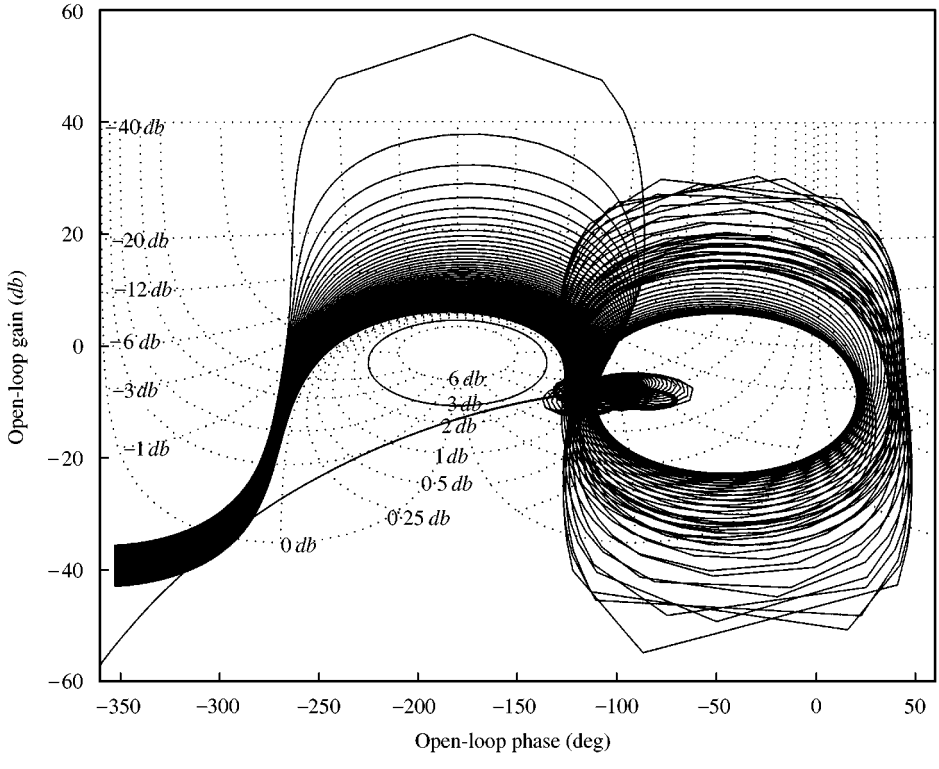

Figure 9. Gain-phase plot of the compensated loop transmission functions for $\tilde{U} \in (1{\cdot}75, 7]$.

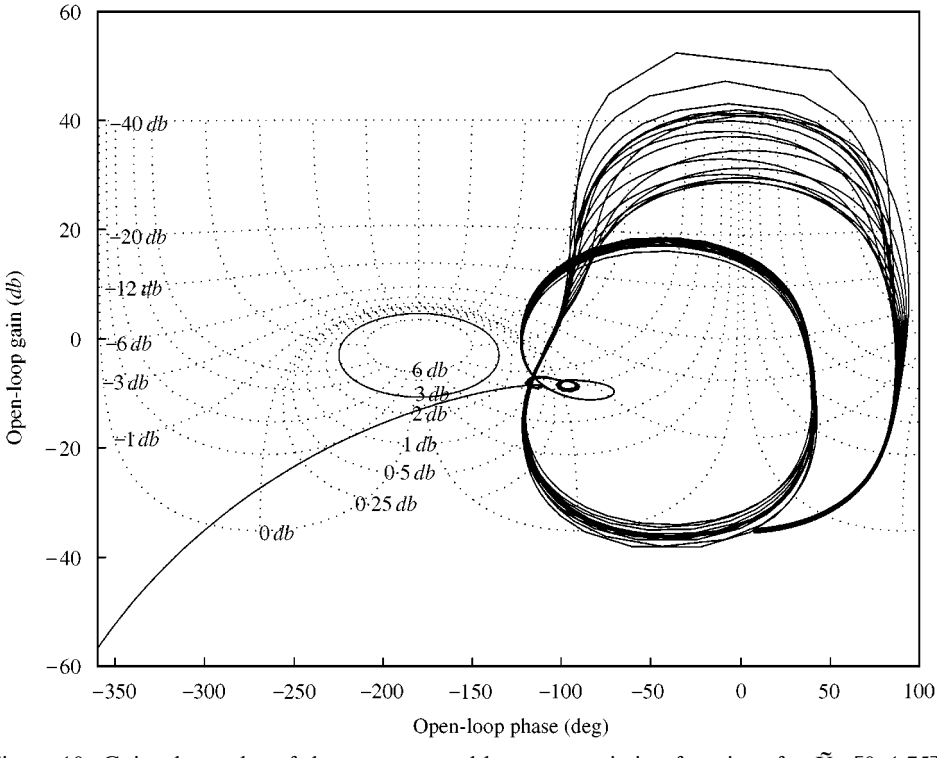

Figure 10. Gain-phase plot of the compensated loop transmission functions for $\tilde{U} \in [0, 1{\cdot}75]$.

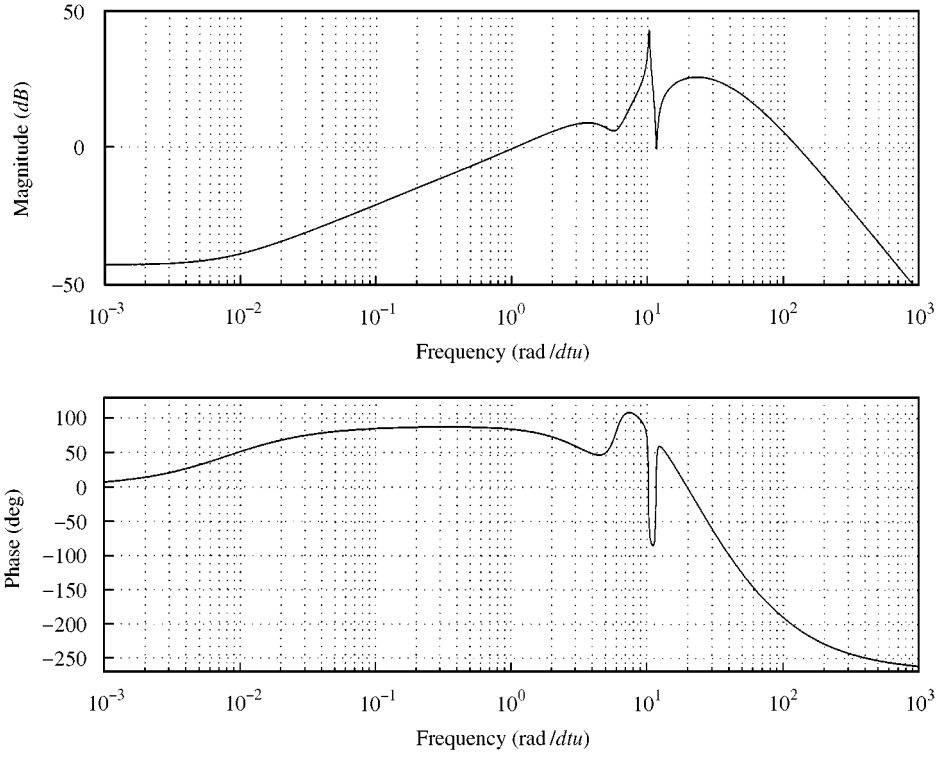

Figure 11. Bode plot of the designed controller.

4.3. TRANSIENT SIMULATIONS

The family of transient responses of the controlled system with the baffle force modelled as a cubic spring and initial conditions $\eta_b = 0{\cdot}0048$ and $\dot{\eta}_b = 0$ for $-T \leqslant \tau \leqslant 0$ is shown in Figure 12. This corresponds to the bifurcation diagram in Figure 3 for $\tilde{U} \in [0, 7]$. The transient responses are allowed to develop without feedback control for 10 dtu, after which the controller is active. From Figure 12, it is evident that complete suppression of the transient vibrations is achieved within 10 dtu. The control effort required to maintain stability at steady-state asymptotically approaches zero.

The family of transient responses of the controlled system with the baffle force modelled as a cubic spring and initial conditions $\eta_b = 0{\cdot}159$ and $\dot{\eta}_b = 0$ for $-T \leqslant \tau \leqslant 0$ is shown in Figure 13. This corresponds to the bifurcation diagram in Figure 4, for $\tilde{U} \in [0{\cdot}7, 2]$. Once again, the transient responses are allowed to develop without feedback control for 10 dtu, after which the controller is active. From Figure 13, it is evident that complete suppression of the transient vibrations is achieved within 10 dtu. Once again, the control effort required to maintain stability at steady-state asymptotically approaches zero.

The family of transient responses of the controlled system with the baffle force modelled as a trilinear spring and initial conditions $\eta_b = 0{\cdot}159$ and $\dot{\eta}_b = 0$ for $-T \leqslant \tau \leqslant 0$ is shown in Figure 14. The transient responses are allowed to develop

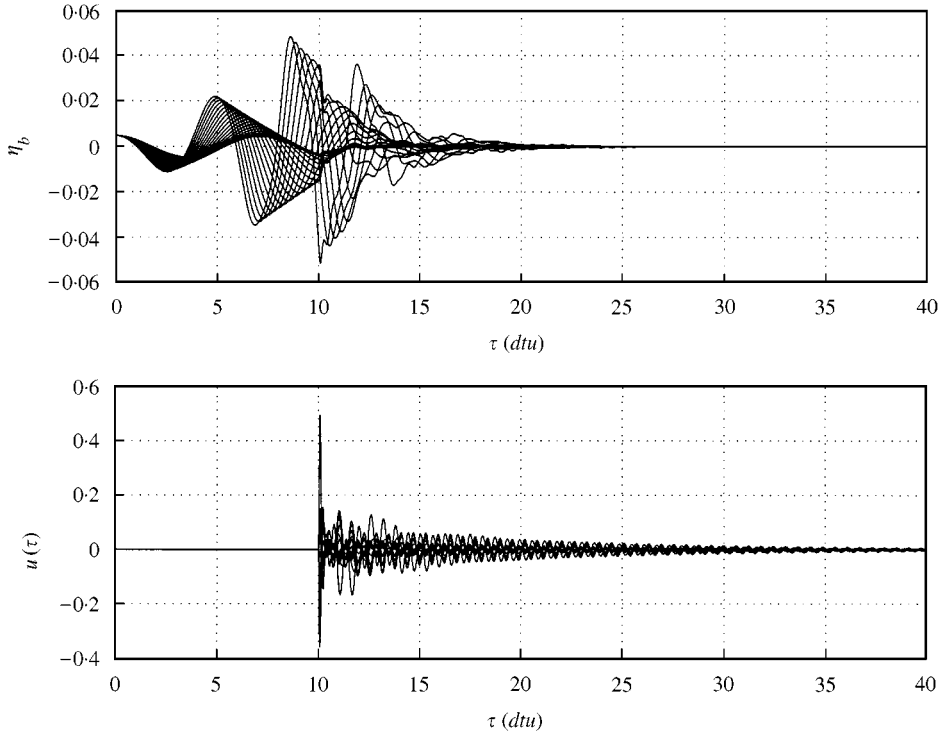

Figure 12. Closed-loop transient response for $\tilde{U} \in [0, 7]$, with small initial conditions (cubic spring model).

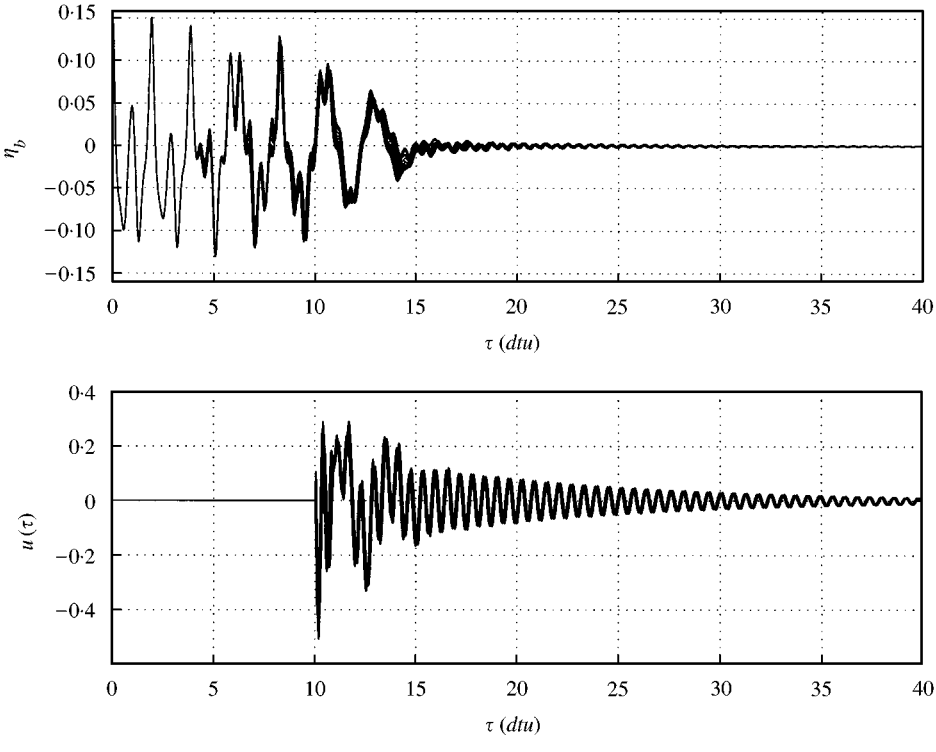

Figure 13. Closed-loop transient response for $\tilde{U} \in [0{\cdot}7, 2]$, with large initial conditions (cubic spring model).

without feedback control for 10 dtu, after which the controller is active. Here again, it can be seen that the unstable motions are suppressed within 10 dtu. Furthermore, the control effort required to maintain stability at steady-state asymptotically approaches zero. The absence of the baffle constraint force for $\eta_b \leqslant 0{\cdot}15$ allows the tube vibration amplitudes to grow larger than the vibration amplitudes from the simulations with the cubic spring model. However, the larger impact force restrains the development of the tube vibration amplitude beyond $\eta_b = 0{\cdot}15$ severely. In fact, the simulations show the gap limits acting as rigid stops.

A final simulation was performed to test the robustness of the closed-loop system to changes in the flow velocity. The transient response of the closed-loop system with the flow velocity incrementally stepped between $0{\cdot}1 \leqslant \tilde{U} \leqslant 7$ is shown in Figure 15. The baffle force is modelled as a trilinear spring and the initial conditions are $\eta_b = 0{\cdot}159$ and $\dot{\eta}_b = 0$ for $-T \leqslant \tau \leqslant 0$. The transient response is allowed to develop without feedback control for 1 dtu, after which the controller is active. From Figure 15, it is evident that complete suppression of the transient vibrations is achieved within 10 dtu. Step changes in the flow velocity have no transient effects on the deflection η_b once the equilibrium position has been reached. Therefore, stability of the uncertain closed-loop system over the entire flow regime $\tilde{U} \in [0, 7]$ has been confirmed.

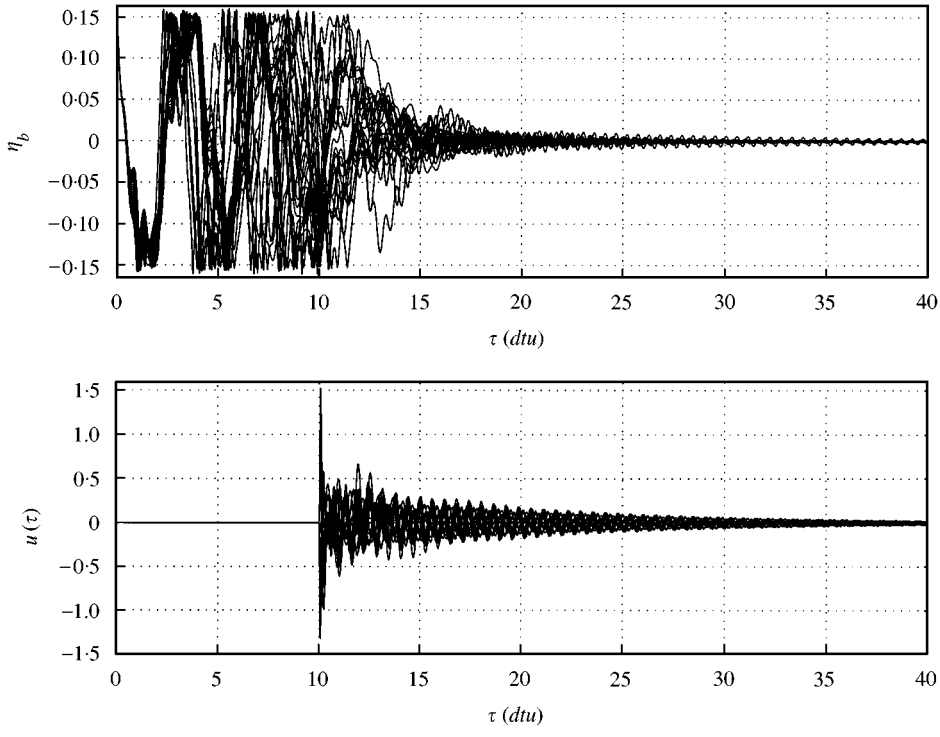

Figure 14. Closed-loop transient response for $\tilde{U} \in [0, 7]$ with large initial conditions (trilinear spring model).

5. CONCLUSIONS

A feedback controller design methodology applied to the flutter-type non-linear vibrations of heat exchanger tubes was developed in this paper. The motivation is to counter the adverse effects of tube and baffle plate impacting on the heat exchanger life. A stability analysis of the system using a cubic spring model for the impacting force was performed to identify flow velocity regimes that required stabilizing control action and performance enhancement. The analysis provided detailed bifurcation diagrams as a function of flow velocity that illustrate the onset of fluid dynamic instabilities, limit cycles and chaotic oscillations of the heat exchanger tube. The stability analysis also identified two additional branches of the bifurcation diagram that arise as a result of large displacements of the heat exchanger tube from its undeformed position.

The feedback controller provided robust closed-loop stability and performance despite a wide variation in the fluid flow velocity. The controller was designed via loop-shaping on the open-loop gain-phase plane such that the Nyquist encirclement condition was satisfied. A closed-loop peak sensitivity performance specification was used to limit the transmission of the external disturbance to the system output. The design approach neglected the additional bifurcation diagram branches and the effects of the restoring baffle impact force by focusing on stabilizing the fluid dynamic instabilities that arise in the system for certain

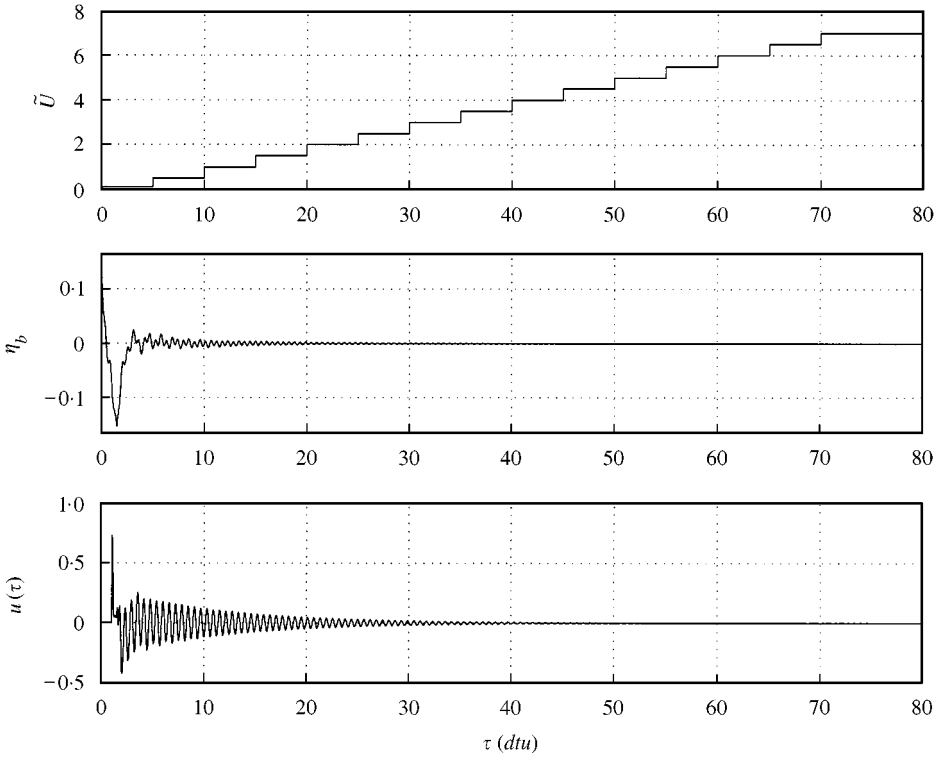

Figure 15. Closed-loop transient response for incrementally stepped $\tilde{U} \in [0, 7]$ (trilinear spring model).

dimensionless flow velocity ranges. Numerical simulation was needed to verify closed-loop stability and performance.

The design of the feedback controller was based on the heat exchanger tube array model which considered all tubes in the array except one to be rigid. For implementation, each heat exchanger tube would need an actuator and sensor, and each tube would have an individual controller. The interaction and cross-coupling that could occur between several loosely fitting tubes has been neglected by this design approach due to the form of the model. However, the only path that can transmit this type of interaction is the fluid medium which would be expected to have a low-pass characteristic. Therefore, this design technique should prove effective for tube array stabilization purposes.

A wide class of continuous systems are required to operate near equilibrium points that are either unstable or have poor stability margins. The controller design approach advanced in this paper can be applied to enhance the stability and performance of these types of systems. For example, flow-induced oscillations in gas turbine engine blades, column buckling under critical loads, and galloping phenomena exhibited in traffic light posts are a few of the systems that could benefit from this controller design technique. Since the closed-loop systems are required to operate near these equilibrium points at steady-state, the control effort required to maintain closed-loop stability at steady-state could be minimal. Therefore,

feedback control could be a viable option for reducing weight and material costs associated with the conventional passive stiffening techniques currently used to address these problems.

REFERENCES

1. S. J. Price and N. R. Valerio 1990 *Journal of Sound and Vibration* **137**, 419–432. A non-linear investigation of single-degree-of-freedom instability in cylinder arrays subject to cross flow.
2. M. P. Paidoussis and G. X. Li 1992 *Journal of Sound and Vibration* **152**, 305–326. Cross-flow-induced chaotic vibrations of heat-exchanger tubes impacting on loose supports.
3. N. W. Mureithi, S. J. Price and M. P. Paidoussis 1994 *Journal of Fluids and Structures* **8**, 833–852. The post-Hopf-bifurcation response of a loosely supported cylinder in an array subjected to cross-flow. Part I: experimental results.
4. N. W. Mureithi, M. P. Paidoussis and S. J. Price 1994 *Journal of Fluids and Structures* **8**, 853–876. The post-Hopf-bifurcation response of a loosely supported cylinder in an array subjected to cross-flow. Part II: theoretical model and comparison with experiments.
5. N. W. Mureithi, M. P. Paidoussis and S. J. Price 1995 *Chaos*, Solitons and Fractals **5**, 847–867. Intermittency transition to chaos in the response of a loosely supported cyclinder in an array in cross-flow.
6. C. H. Yau, A. K. Bajaj, and O. D. I. Nwokah 1995 *Journal of Fluids and Structures* **9**, 99–122. Active control of chaotic vibration in a flexible pipe conveying fluid.
7. D. H. Chyung and E. Bruce Lee 1966 *Journal of SIAM Control* **4**, 548–575. Linear optimal systems with time delays.
8. H. N. Kouivo and E. Bruce Lee 1972 *Automatica* **8**, 203–208. Controller synthesis for linear systems with retarded state and control variables and quadratic cost.
9. N. Luo and M. de la Sen 1992 *Proceedings of the American Control Conference*, 894–895. State feedback sliding mode control of a class of uncertain time delay systems.
10. N. Luo, M. de la Sen and J. Rodellar 1997 *International Journal of Robust and Nonlinear Control* **7**, 59–74. Robust stabilization of a class of untertain time delay systems in sliding mode.
11. J.-H. Ge, P. M. Frank and C.-F. Lin 1996 *Automatica* **32**, 1183–1185. Robust H^{∞} state feedback control for linear systems with state delay and parameter uncertainty.
12. J. H. Lee, Y. S. Moon and W. H. Kwon 1996 *Proceedings of the* 35*th Conference on Decision and Control*, 2092–2096. Robust H^{∞} controller for state and input delayed systems with structured uncertainties.
13. O. Toker and H. Ozbay 1993 *Proceedings of the* 32*nd Conference on Decision and Control*, 1170–1175. H^{∞} controllers for unstable distributed plants.
14. H. W. Bode 1945 *Network Analysis and Feedback Amplifier Design*. New York: Van Nostrand Reinhold.
15. M. A. Franchek and P. Herman 1998 *International Journal of Robust and Nonlinear Control* **8**, 1021–1042. Direct connection between time domain performance and frequency domain characteristics.
16. J. M. Maciejowski 1989 *Multivariable Feedback Design*, pp. 31–33. New York: Addison-Wesley.